Hindawi
Geofluids
Volume 2023, Article ID 9497320, 12 pages
https://doi.org/10.1155/2023/9497320

*Research Article*

# The Prototype Test on Sealing Capacity and Mechanical Behavior of the Underground Segmental Lining in a Low Vacuum Environment

**Qianqian Lv**,[1,2] **Chuigang Zeng**,[1,2] **Fengyuan Li**,[1,2] **Kui Chen**,[1,2] **Long Shi**,[3] **and Ruixiang Chen**[1,2]

[1]*State Key Laboratory of Shield Machine and Boring Technology, Zhengzhou 450001, China*
[2]*China Railway Tunnel Group Co., Ltd, Guangzhou 511458, China*
[3]*Southwest Jiaotong University, Chengdu 610031, China*

Correspondence should be addressed to Qianqian Lv; 674936740@qq.com

Received 27 September 2022; Revised 30 November 2022; Accepted 1 April 2023; Published 28 April 2023

Academic Editor: Zhengzheng Xie



The super-speed tube transport (SSTT) system is called the fifth traffic mode internationally. One of the critical technical problems for the design of SSTT system is the sealing reliability in vacuum tube structures. In this paper, an experimental study of the sealing capacity and mechanical behavior of the segmental lining is carried out, and the following conclusions are drawn. To meet the requirements of the SSTT system, the existing sealing of the concrete segment structure needs to be further strengthened. The joint spacing decreases with increasing vacuum and increases with vacuum pressure relief. There is an obvious correlation between the strain change and the vacuum pumping, which can be divided into four stages. The influence of the pressure difference and the local airflow movement on the concrete surface strain is dominant by turns at different stages. The concrete surface is suggested to be reinforce on account of the tensile strain caused by the local airflow movement of vacuum pumping is significant. The relative pressure caused by vacuum has little effect on the stress and deformation of the structure. The results of the study can help to understand the sealing capacity and mechanical behavior of the underground segmental lining in a low vacuum environment and be beneficial in choosing the appropriate structure type for the SSTT system.

## 1. Introduction

The running speed of the existing railway transportation is restricted by air resistance, wheel-rail friction, and running noise [1, 2]. These problems can be solved by magnetic levitation technology, which can reduce the wheel-rail friction and vibration, as well as by building a low-vacuum operating environment to reduce air resistance and noise, i.e., the super-speed tube transport (SSTT) system, which is called the fifth traffic mode internationally [3–6]. At present, the maglev train technology in Germany, Japan, China, etc. has been mature, and the Hyper Loop project in the United States has also been placed on the practice agenda concretely.

The concept of SSTT was put forward in detail by the ET3 company. In 1999, the ET3 company was registered by an American engineer Daryl Osterfor who applied for the invention patent of the vacuum pipeline transportation system [6, 7]. The structure of the low-vacuum pipeline has been tried in different projects. In the Virgin Hyperloop One scheme in America, a carbon steel pipeline with a diameter of 3.3 m was used. A test with a maximum speed of 387 km/h was conducted in December 2017, and the first manned test of the ultra-high-speed vehicle was successfully conducted in November 2020 [8–12]. In the Swissmetro scheme of Switzerland, the design of a single-hole single underground line was adopted, and the reinforced concrete tunnel structure with a diameter of 5 m was used [13, 14]. In the TransPod scheme in Canada, a 4 m-diameter steel pipe was used, which was connected to the pier cap through steel supports [15]. It has also developed rapidly in China in recent years. The first vacuum tube experimental platform of

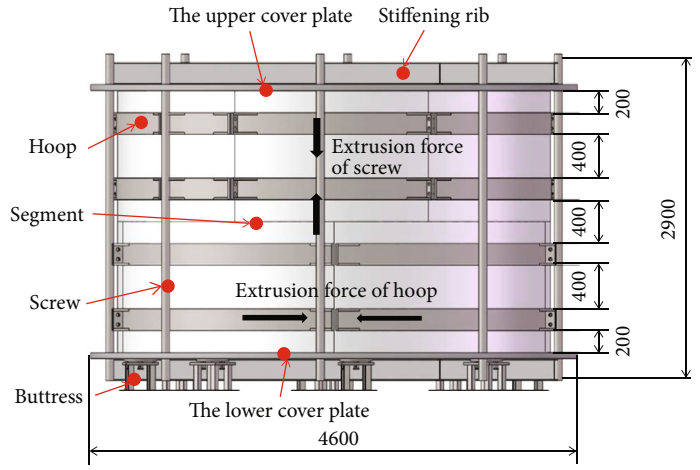


Figure 1: The vertical assembly scheme of double ring segment (unit: mm).

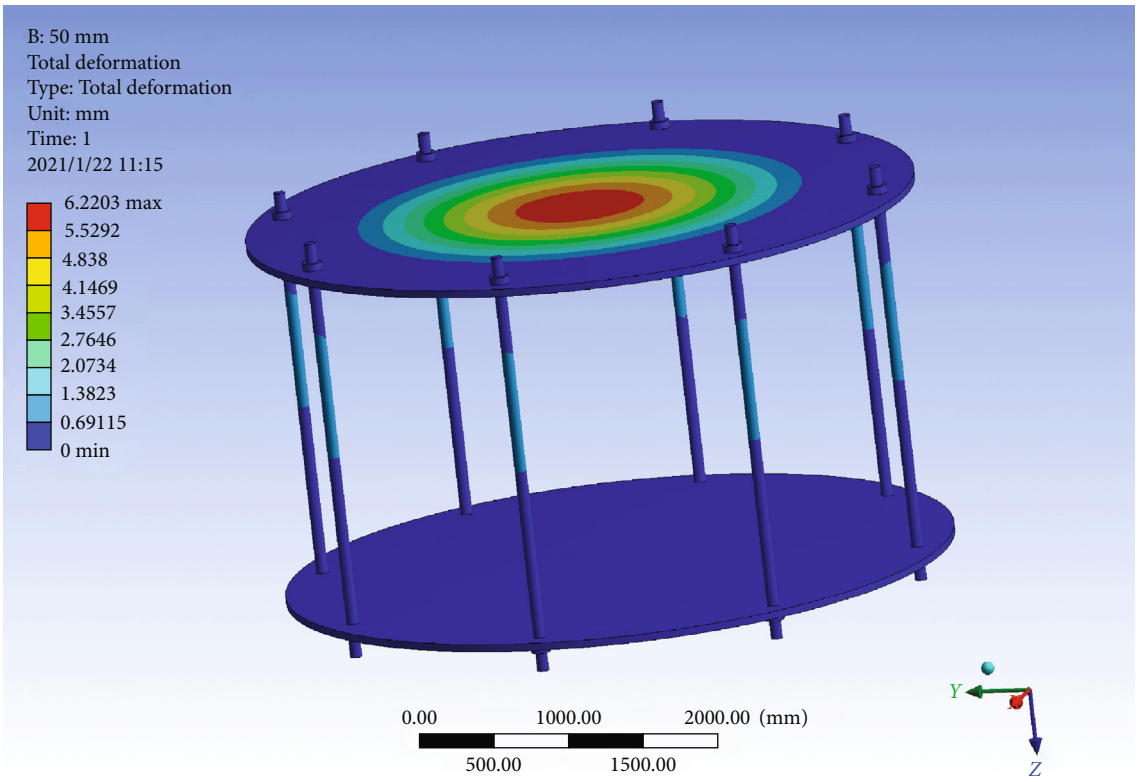


Figure 2: The deformation of 50 mm thick steel plate.

the high-temperature superconducting maglev vehicle Super-Maglev was constructed and debugged successfully in June 2014 by Southwest Jiaotong University, which integrated the traction, communication, and stepdown tests [16–18]. In January 2021, the first prototype test line of high-temperature superconducting maglev was officially launched in Chengdu, Sichuan. In this test, the technology of Southwest Jiaotong University was used. Besides, the normal magnetic levitation model vehicle with the top speed of 600 km/h was successfully offline by CRRC Sifang in July 2021. Hunan Yuanda Group also carried out the related system research, and the vacuum pipeline adopted the steel core plate welding. In this scheme, the cross section of the vacuum sealing structure was double-layered, and the corrugated pipe was used at the connection between pipes.

At present, there are many restrictions on the SSTT, one of which is the low vacuum pipeline. To build a safe vacuum pipeline environment, the mechanical properties as while as the sealing reliability of pipeline structure are critical factors. Using the existing tunnel segment lining of the subway system is more in accordance with the actual situation [19]. Then the sealing capacity of underground engineering becomes the key problem. Gong et al. [20] proposed a novel numerical approach to simulate the localized leakage of

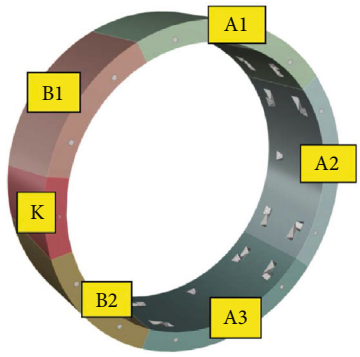


Figure 3: Construction plan of segment.

segmental linings, finding that the internal forces were substantially affected by the seepage rate. Lei et al. [21] conducted a combined investigational, experimental, and computational research on the gasket sealing capacity of joints with different joint deformations in cross-river shield tunnels. To evaluate the airtightness of concrete as a material for the SSTT system, Park et al. [22, 23] established a correlation analysis between the crack development in a concrete tube structure and the internal pressure change. It can be seen that researches above are mainly concentrated on normal pressure conditions or pipeline without joints. Therefore, it is of great significance theoretically and practically to study the mechanical properties of the existing segment structure under low vacuum condition for the development of the fifth traffic [24–27]. By conducting the indoor experimental on a prototype platform, this study is aimed at researching on the sealing capacity and mechanical properties of tunnel segment structure in a low vacuum environment and providing a basis for pipeline structure selection of low vacuum pipeline transportation system.

## 2. Segment Prototype Test Design

*2.1. Test Purpose.* To study the mechanical properties of the tunnel segment structure under low vacuum condition, a prototype segmental lining with low vacuum test system was designed to simulate the working conditions of the construction site.

*2.2. Test Component Design.* The difference between the horizontal and vertical assembly of the segment rings is whether the effect of gravity on the joint is uniform. Under the test conditions, the segment diameter is smaller, and the integrity of the segment ring is better under the action of hoop and pull rod, so the difference of joint state under gravity is smaller. Considering the safety and cost of the test, the segment was vertically assembled.

The scheme of the test was designed as follows: the two ring segments were assembled vertically, and the ends on both sides were sealed with circular thick steel plates effectively. The screw was used to apply the extrusion force of the sealing gasket between the segment rings in the actual working condition, and the circumferential hoop was used to apply the extrusion force of the sealing gasket between

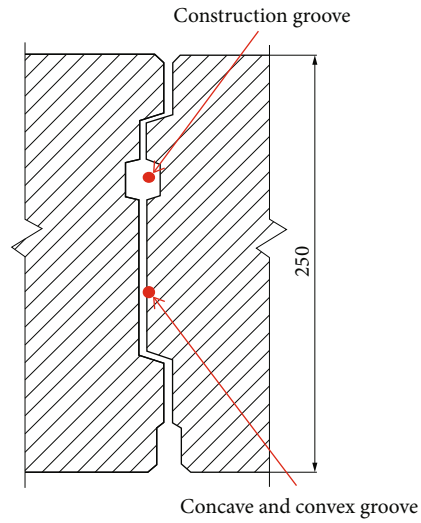


Figure 4: The longitudinal joint (unit: mm).

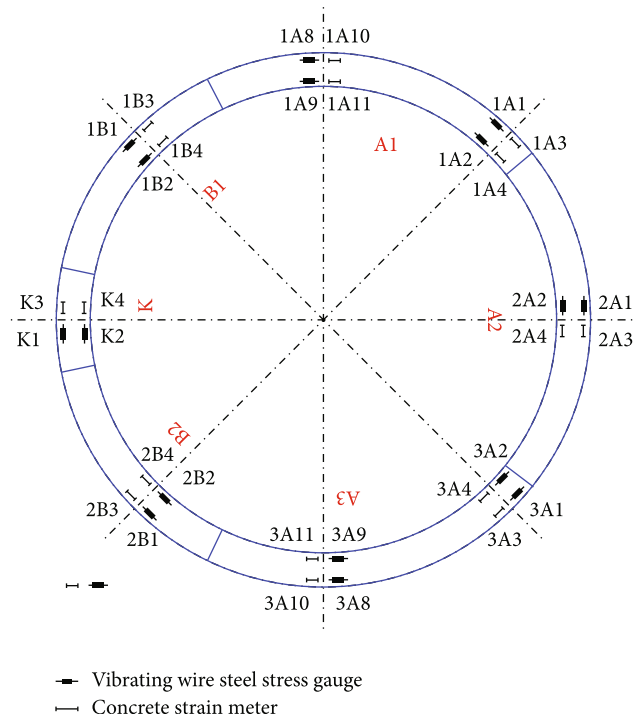


Figure 5: Diagram of installation position of embedded sensors.

the segments, as shown in Figure 1. The upper steel plate was perforated and connected to the pumping pipeline of the vacuum pump. The sealing method was consistent with the conventional shield tunnel segment, and the compression force of the sealing gasket was $f = 80\,\text{kN/m}$ according to the actual situation.

To form a closed space, the upper and lower steel plates were used to cover the two ring segments. A three-dimensional model was established to check the strength of the steel plate. The whole compression force of the seal ring is $F = 2f \cdot S = 2f \cdot 2\pi R = 2 \times 80kN/m \times 2 \times 3.14 \times 2\,m = 201\,t$. In the formula, $R$ is for the radius of the segments, and $f$

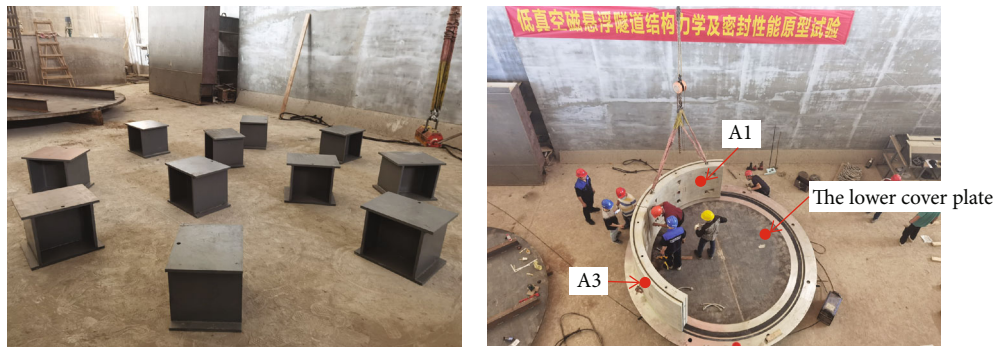


(a) The placement of buttresses (b) The installation of the lower ring segments

Figure 6: Field photo of segment assembly.

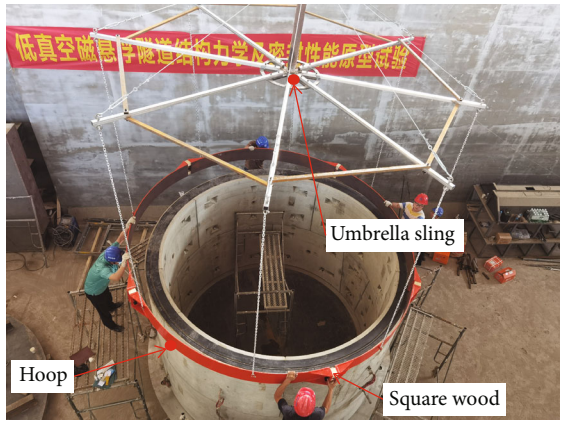


Figure 7: Hoop installation.

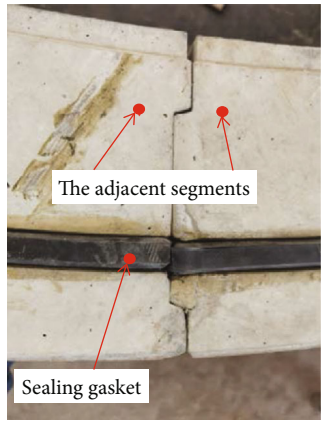


Figure 8: Alignment of adjacent segment gaskets.

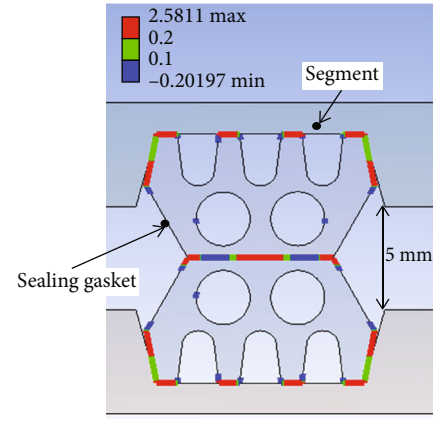


Figure 9: Contact pressure at the joint.

is for the compression force per meter of the unilateral seal ring. In the model calculation, the weight was taken into account, and the bottom boundary of the model was fixed. The deformation and stress distribution of steel plates with the thickness of 20 mm, 30 mm, and 50 mm were obtained by modeling calculation. The corresponding maximum displacements were 89.04 mm, 27.04 mm, and 6.22 mm, respectively, and the maximum stresses were 787.39 MPa, 354.62 MPa, and 144.68 MPa, respectively. The deformation of steel plates with a thickness of 50 mm is shown in Figure 2.

It can be seen the 50 mm steel plate was needed to decrease the deformation. The outer diameter of the steel cover was 4.5 m, Q355 alloy steel was used, and the stiffening rib used $200 \times 100$ I-section steel. The contact surface between the steel plate and the segments was pasted with a 5 mm-thick EPDM rubber pad. There were 2 vents and 3 aviation socket installation holes at the upper cover plate. To provide the working space and make the structure level, the overall segment rings were supported by the buttresses.

The screws were used to apply the extrusion pressure of the gaskets in the annular gap of the segments. There were 8 screw holes along the circumference of the steel cover plates. The diameter of the screw was 75 mm, the length was 2.9 m, and the strength class was 12.9.

The hoops were used to apply the extrusion pressure of the gaskets at the longitudinal joints. The thickness of the hoop steel plate was 10 mm, the width was 20 cm, and the steel type was Q345B. The hoop was divided into 6 segments consistent with the segment ring, and the segments of each hoop were connected by two $M30 \times 80$ bolts. The hoop joint was strengthened by a 20 mm-thick steel plate rib. The weld seam at the joint was double-sided welding with equal strength and passed 100% nondestructive testing. There

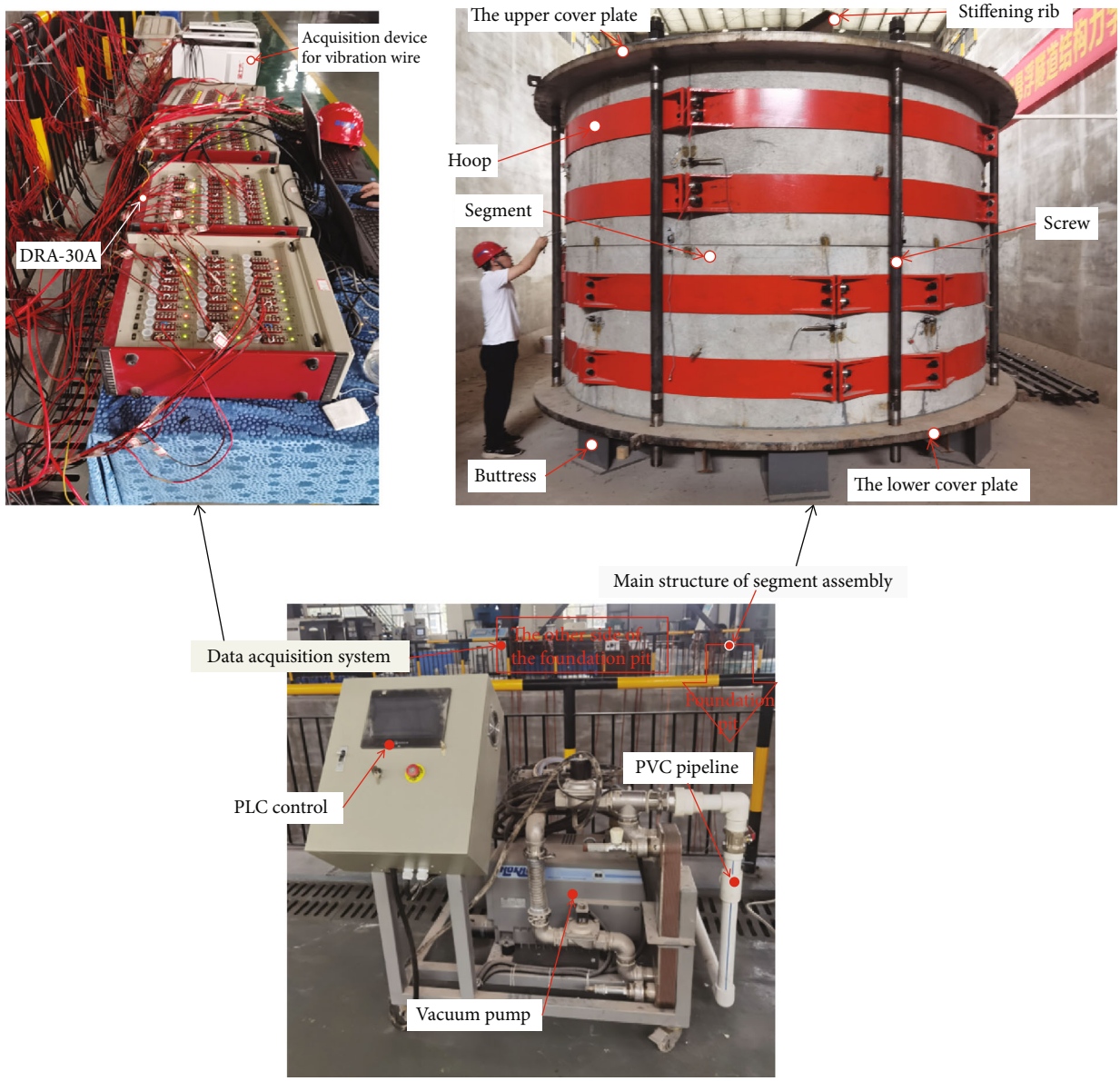


Figure 10: Field photo of the segment assembly.

were four hoop laps in total; the upper and lower segments each had two laps, as shown in Figure 1.

The inner diameter of the test segment was 3.5 m, and the outer was 4.0 m. The concrete class was C50, the impermeability grade was P10, the thickness of the segment was 250 mm, and the width of the segment ring was 1200 mm. The segment along the ring was divided into 6 blocks, namely, the capping block (K), adjacent block (B1/B2), and standard block (A1/A2/A3), as shown in Figure 3.

There were concave and convex grooves at the longitudinal joints of the segments, as shown in Figure 4. The segments were connected by curved bolts: twelve M24 bolts in the circumferential direction and fourteen M24 bolts in the longitudinal direction. The steel type of the bolts was HRB400. The lining ring of the shield tunnel was a double-sided wedge-shaped universal ring with a wedge amount of 18 mm.

*2.3. Sensor Layout.* The two ring segments were monitored in the test. The embedded sensors were arranged at eight equal angle-monitoring points of each ring segment. There were two vibrating wire steel stress gauges and two concrete strain gauges at each monitoring point. They were installed horizontally on the main reinforcements in the segments, as shown in Figure 5. The maximum range of the reinforcement meter was 40 kN, and the sensitivity was $2.5 \times 10^{-5}$kN/Hz$^2$. The maximum range of the concrete strain gauge was 1500 $\mu\varepsilon$, and the sensitivity was $4 \times 10^{-4}$ $\mu\varepsilon$/Hz$^2$.

The strain gauges were pasted at the joints. The strain gauge model was BX120-20AA, the resistance was 120 ohm, the length of the sensitive grid was 20 mm, the width was 3 mm, the sensitivity coefficient was 2.08, and the maximum range was 20000 microstrain. After being fixed with 502 glue, it was reinforced with epoxy resin AB sealing layer.

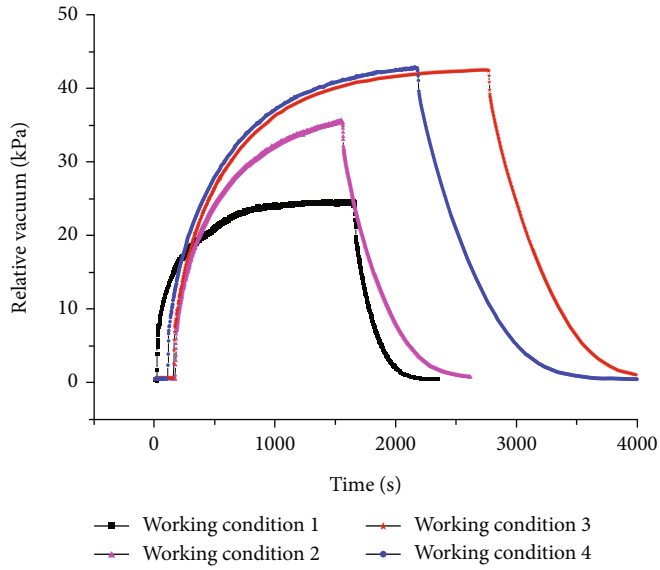


Figure 11: The vacuum degree along with time.

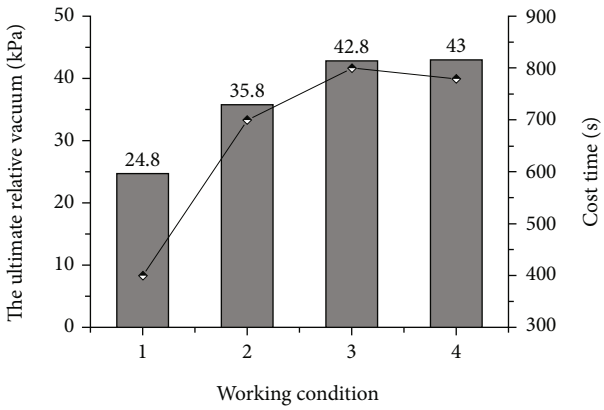


Figure 12: The ultimate vacuum degree and cost time.

The displacement meters were also installed at the joints, and the range was 20 mm with an accuracy of 1%.

To ensure that the pretightening force exerted by the screws and hoops met the requirements of the test conditions, a strain bolt axial force meter was installed at the nut.

The multichannel digital strain meter DRA-30 A was used to collect the data of the axial force meter, strain gauge, and resistance displacement meter. The data of embedded steel and concrete stress meter was collected by multichannel vibrating wire acquisition instrument.

## 3. Prototype Segment Test System Construction

*3.1. Segment Assembly.* Firstly, the buttresses were placed at the present position, as shown in Figure 6(a).

Next, the lower steel cover plate was lifted into place and adjusted horizontally. Then, the gasket was fixed between the lower cover plate and segments.

The installation of the lower ring segments started from the A3 block, followed by the A1/A2, B1/B2 symmetrical assembly, and finally the K block, as shown in Figure 6(b). When installing adjacent segments, the bolts were preloaded first and retightened after the segments were ringed.

The assembly point of the upper ring segment was rotated 180° relative to the lower ring, and the assembly sequence was the same as that of the lower ring segment. After each segment was in place, the circumferential and longitudinal seam bolts were pretightened and fixed. The bolts were retightened twice when the whole ring assembly had been completed.

The hoop was assembled on the ground before installing. To ensure that the hoop could be smoothly sleeved into the segment ring, a customized umbrella sling was used for lifting, as shown in Figure 7.

The upper cover plate was hoisted after the top sealing rubber pad had been fixed. There was a maintenance manhole with a diameter of 80 cm at the upper cover plate. The screw was hoisted into the hole of the cover plate and fixed with the double nut.

The gaskets between the upper and lower ring segments were aligned, as well as the gaskets between the adjacent blocks, as shown in Figure 8. The diameter error of the ring segment was within 2 mm.

The numerical simulation analysis of the joint gasket was carried out. In the model, a planar strain linear element and triangular mesh were used. The Mooney-Rivlin two-parameter model was adopted to simulate the sealing gasket, and the value of the hardness was 65°. The contact pressure distribution at the joint with a 5 mm opening is shown in Figure 9.

In Figure 9, the contact pressure in the blue area was less than 0.1 MPa, which can be regarded as an invalid sealing area, and the contact pressure in other areas was greater than 0.1 MPa, which can be regarded as an effective sealing area.

It can be seen that when the opening amount of the gasket reached 5 mm, the sealing of the structure had not been affected theoretically. When the diameter error of 2 mm was

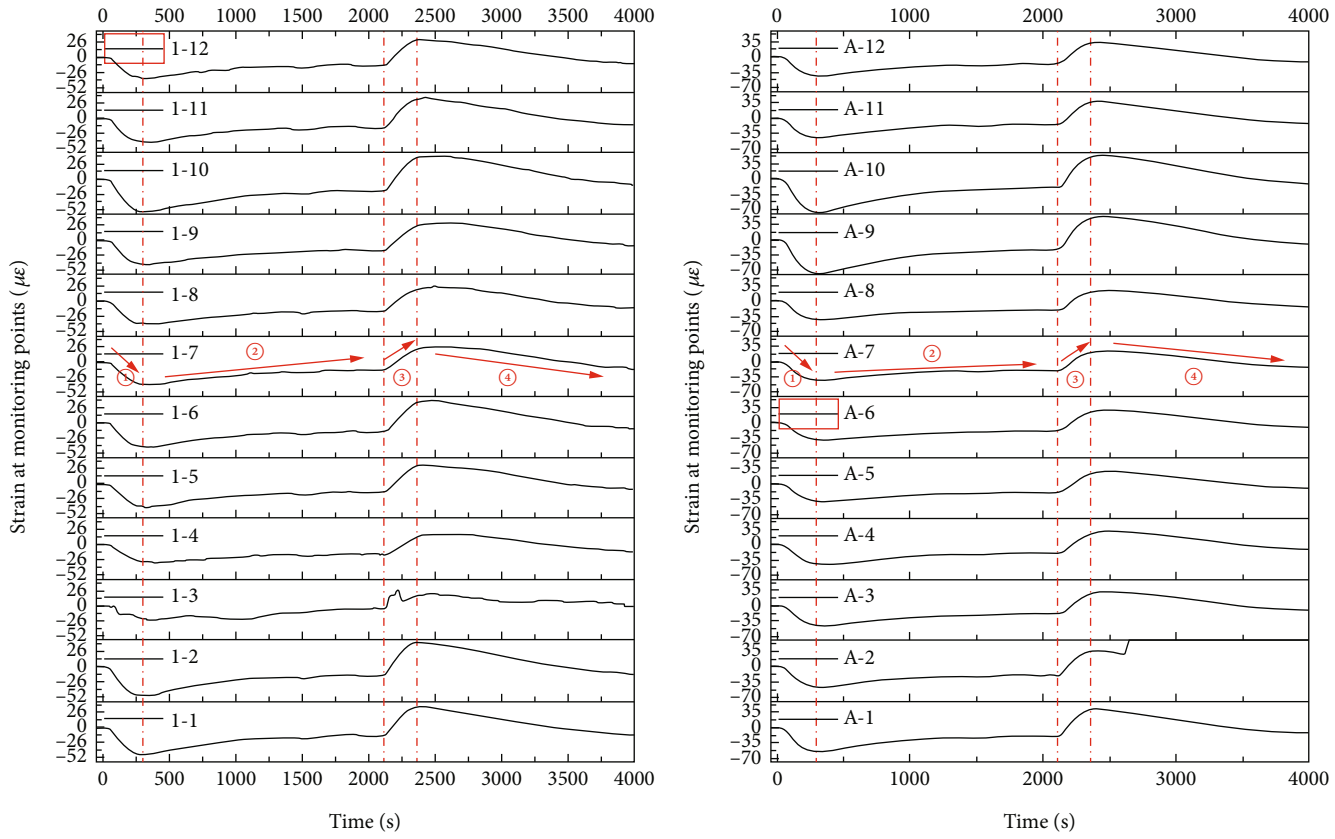


(a) Series 1 (b) Series A

Figure 13: Strain curve along with time at monitoring points.

averaged to the 6 longitudinal joints, the opening amount of each elastic gasket was 0.33 mm. Thus, the assembly error would not affect the sealing performance of the structure.

*3.2. System Connection Debugging.* After the installation of the main structure was completed, as shown in Figure 10, then came the sensor installation and line connection, vacuum pump pipe connection, and installation.

A rotary vane vacuum pump with a pumping rate of 200m$^3$/h was chosen. The PVC pipe with a 50 mm diameter was led from the reserved port of the upper cover plate to the vacuum pump outlet.

To verify the boundary seal between the segment ring and the steel cover plate, the air pump was used, and the soap liquid was coated at the joint between the segment ring and cover plates. The air pump was started to make the cavity of the segment rings at a positive pressure of 10 kPa. If soap bubbles appear, it was necessary to strengthen the seal. If not, the test could be carried out.

## 4. Prototype Test of Low Vacuum Segment

Referring to the actual situation on site, the compression force of the sealing ring $f$ was taken as 80 kN/m, and the ring width was 1.2 m. Each ring segment had two hoops, so the axial force of the hoop was taken as $f = (80\text{kN/m} \times 1.2\,m)/2 = 48\text{kN}$. The maximum tension of the vertical screws was 80 kN, and the direction of the applied force is shown in Figure 1. The test is carried out in four working conditions.

Working condition 1: natural assembly state. After the segment assembly was completed, the joints of the segments were pretightened, mainly through the assembly bolts. It was confirmed that the axial force meters of the screws and hoops were at zero

Working condition 2: the tension of the vertical screws was adjusted to 40 kN, while the axial force of the hoop was 0. At this time, the longitudinal assembly force was simulated by using the pressure of the screw

Working condition 3: the tension of the vertical screws was adjusted to 80 kN, and the axial force of the hoop is 0

Working condition 4: the tension of the vertical screws was adjusted to 80 kN, and the axial force of the hoop was 48 kN. The hoop force was used to approximate the transverse assembly force

After the axial force of the vertical screws and annular hoops was adjusted to a specific working condition, keep the vacuum pump working until the vacuum degree no longer rises. The relative vacuum degree curve with time is shown in Figure 11. Noting that the relative vacuum degree in this paper refers to the difference between the pressure of the atmosphere and the measured object.

As can be seen from Figure 11, when the screw axial force was increased to 40 kN, the ultimate vacuum degree in working condition 2 was significantly improved

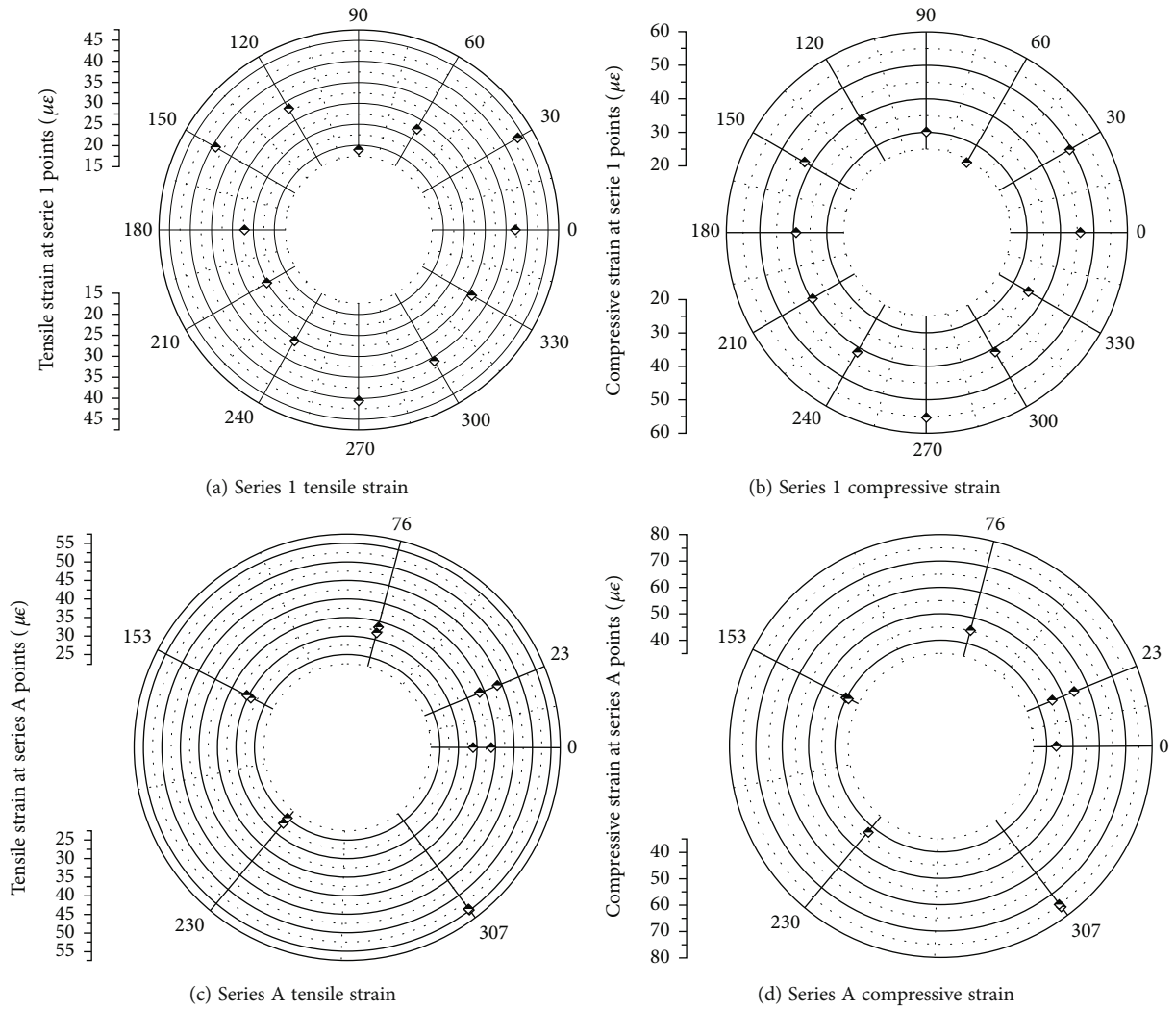


(a) Series 1 tensile strain

(b) Series 1 compressive strain

(c) Series A tensile strain

(d) Series A compressive strain

Figure 14: Distribution of maximum strain at each monitoring point.

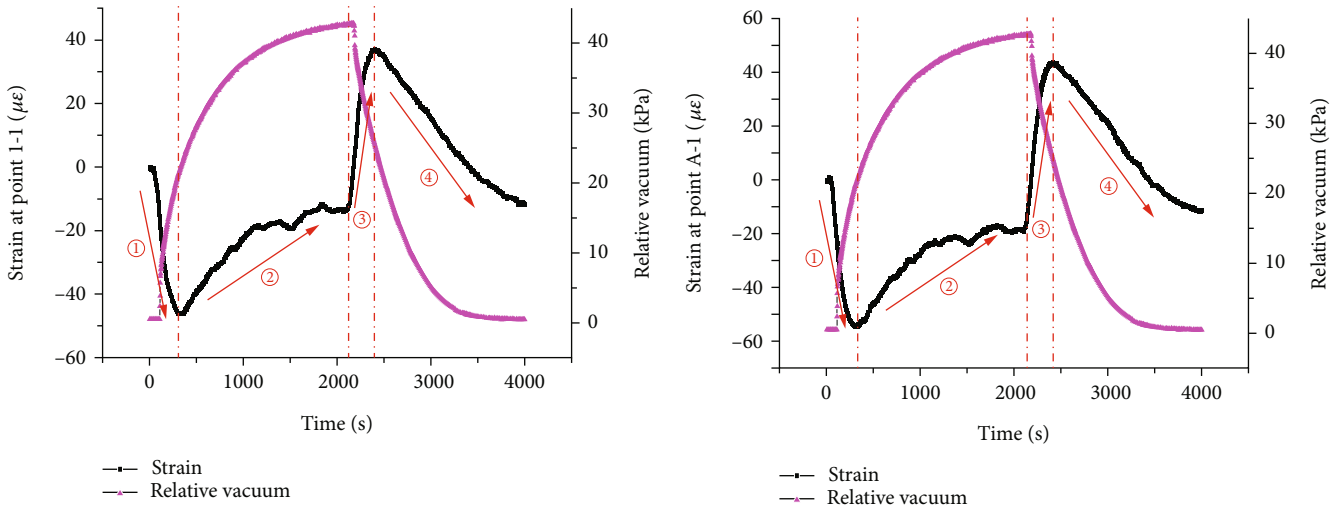


(a) 1-1

(b) A-1

Figure 15: Curve of strain and vacuum degree along with time.

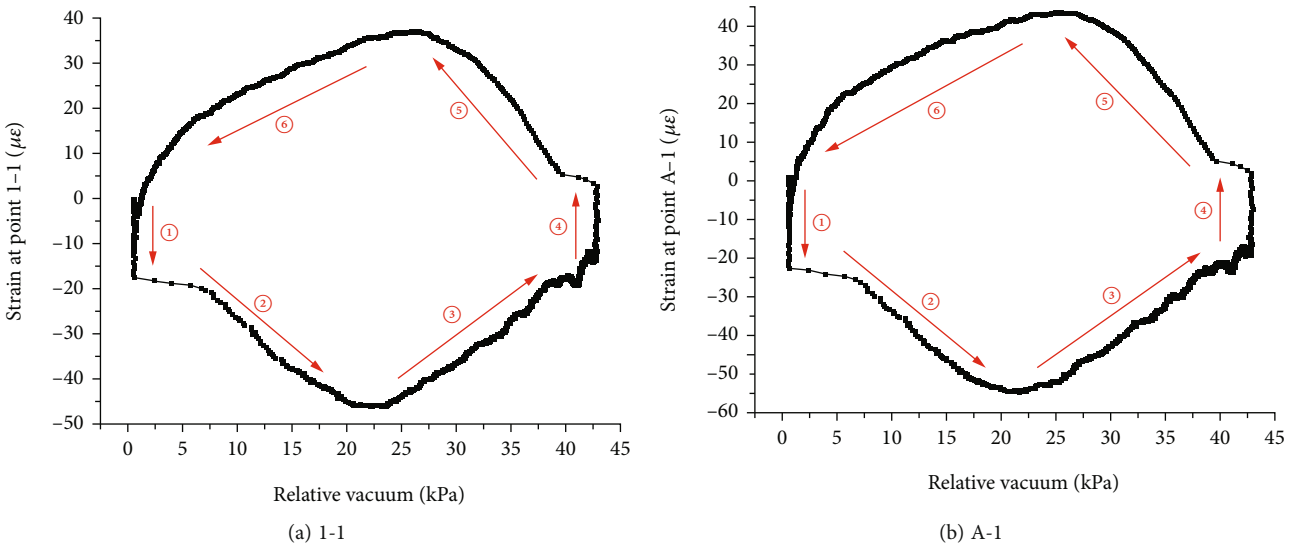


Figure 16: Strain curve along with vacuum degree.

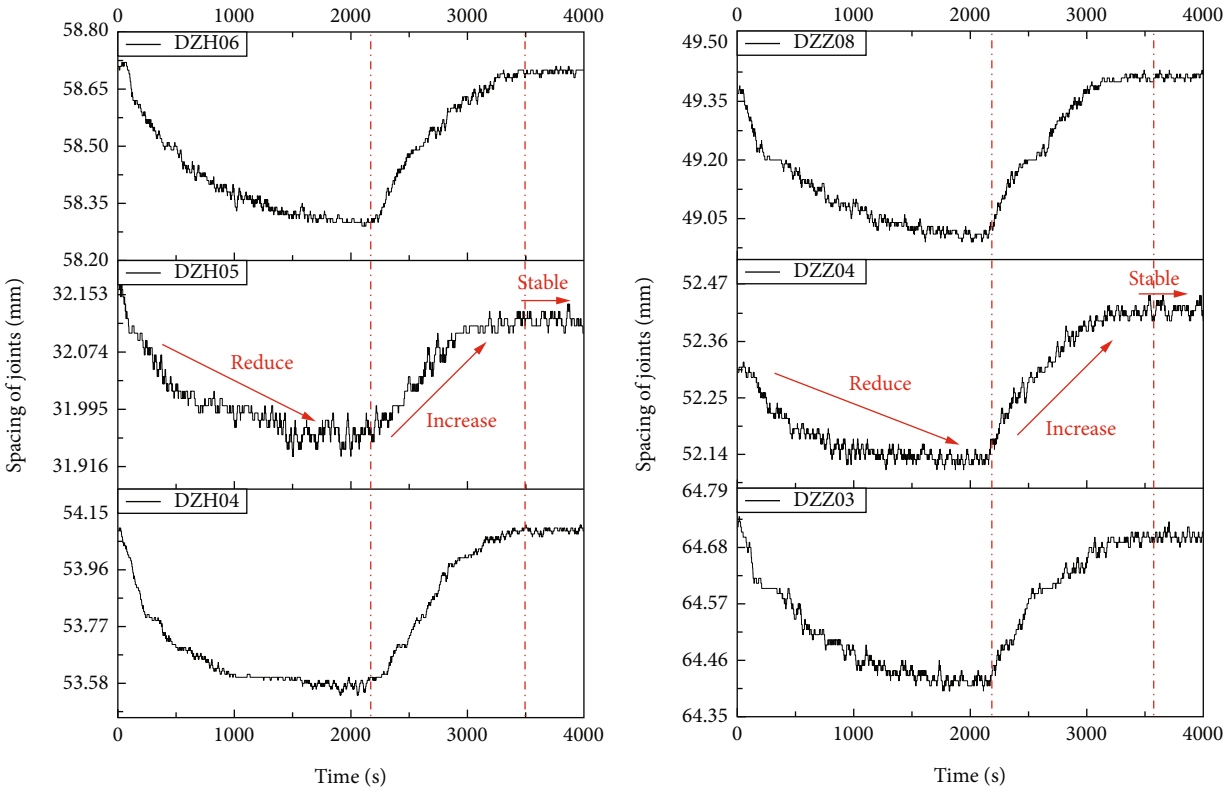


Figure 17: Curve of joint spacing along with time.

compared with that in working condition 1. And when the screw axial force is increased to 80kN, the ultimate vacuum degree in working condition 3 is further improved compared with that in working condition 2. But when the axial force of the hoop was increased to 48 kN, there was no obvious difference between the ultimate vacuum degree in working condition 3 and working condition 4. It can be seen that increasing the screw tension is conducive to improve the air tightness of the structure, while the tension of the hoops has a limited effect on the improvement of the structural seal.

In working condition 4, the relative vacuum degree increased rapidly in the early stage (reaching a semipeak in 300 s) and then increased slowly. The relative vacuum reached a maximum value of 43 kPa around 2000 s. There was a balance between the pumping efficiency and the leakage speed of the assembled segment structure at this

Table 1: Maximum stress of reinforcing bar at monitoring point.

| Monitoring point | Initial frequency $f_1$ | Working frequency $f_2$ | Stress (kN/m$^2$) |
|---|---|---|---|
| K2 | 1460 | 1453 | 25.21 |
| 2B1 | 1410 | 1407 | 10.98 |
| K2 | 1805 | 1796 | 42.08 |
| 1A1 | 1354 | 1353 | 3.50 |
| 1A2 | 1412 | 1409 | 10.60 |
| 1A8 | 1333 | 1330 | 10.40 |
| 1A9 | 1368 | 1359 | 29.88 |
| 2A2 | 1469 | 1459 | 35.42 |
| 3A2 | 1448 | 1446 | 7.12 |

Table 2: Maximum strain of concrete at monitoring point.

| Monitoring point | *Initial frequency* $f_1$ | Working frequency $f_2$ | Compressive strain $\varepsilon$ ($\mu\varepsilon$) |
|---|---|---|---|
| K3 | 2221 | 2215 | 10.96 |
| 1A3 | 2189 | 2186 | 5.26 |
| 1A10 | 2210 | 2207 | 5.23 |
| 1A11 | 2199 | 2188 | 19.48 |
| 2A4 | 2260 | 2249 | 20.57 |
| 3A4 | 2202 | 2200 | 3.56 |

moment, meaning the ultimate vacuum of the test system had been achieved. After closing the vacuum pump, due to the leakage of the structure, the relative vacuum decreased rapidly and went back to atmospheric pressure after 1500s.

Figure 12 shows the ultimate vacuum degree and the cost time to reach 80% of the ultimate vacuum under different working conditions. It can be seen that the ultimate vacuum degree and cost time increased successively in the first three working conditions, but there was no significant difference between working condition 3 and working condition 4.

The data of the monitoring points during the vacuum pumping process in working condition 4 is analyzed as follows.

*4.1. Strain Monitoring.* The monitoring points on the outer surface were affected less by the vacuum through the comparison of experimental data, so significant attention was paid to the strain gauge on the inner surface. The gauge strain data on the inner surface is shown in Figure 13. Among them, 1-1~1-12 were the longitudinal strain gauges, which were located at the 12 equal points of the ring joint, referred to as 1 series monitoring points hereinafter; A-1~A-12 were circumferential strain gauges, located in the middle of the six longitudinal joints on both sides, referred to as A series monitoring points.

It can be seen from Figure 13 that during the vacuuming process, each longitudinal monitoring point has a similar strain tendency with time. Due to the fact that the concrete material is isotropic.

It can be seen that the maximum tensile strain of Series 1 was 43.65 $\mu\varepsilon$ in Figure 14(a), and the compressive strain was 55.3 $\mu\varepsilon$ in Figure 14(b). While the maximum tensile strain of Series A was 54.8 $\mu\varepsilon$ in Figure 14(c) and the compressive strain was 75.8 $\mu\varepsilon$ in Figure 14(d). The circumferential and longitudinal intervals were close. The maximum compressive strain range was 55.3 $\mu\varepsilon$~75.8 $\mu\varepsilon$, and the maximum tensile strain range was 43.65 $\mu\varepsilon$~54.8 $\mu\varepsilon$. The compressive strain was greater than the tensile strain. The maximum compressive strain of the ring was about 2% of the ultimate compressive strain (0.0033), and the maximum tensile strain was about 55% of the ultimate tensile strain (0.0001) of concrete.

From Figures 15(a) and 15(b), it can be seen that there was a significant correlation between the strain change and the vacuum pumping. As shown in Figure 15(a), it was divided into four stages. In the first stage, with the rapid increase in the relative vacuum degree, the compressive strain value increased and reached 45.8 $\mu\varepsilon$ at 300 s. In the second stage, as the change of vacuum degree tends to be gentle, the compressive strain decreased to zero, and the airflow of leakage and pumping reached to a balance. In the third stage, at the initial stage of vacuum relief, the tensile strain increased rapidly (the tensile strain increased by about 40 $\mu\varepsilon$ in 2100 s ~2300 s. In the fourth stage, the relative vacuum tended to zero and the tensile strain decreased.

From Figures 16(a) and 16(b), it can be seen that with the vacuum process, the relative vacuum degree increased first and then decreased, and the strain change curve was approximately divided into six broken lines. In the first and fourth stages, the relative vacuum degree remained unchanged while the strain increased, showing the change of vacuum degree lagged behind the strain. In the second stage, with the increase of relative vacuum degree, the compressive strain increased. In the third stage, with the relative vacuum degree increased gently, the compressive strain decreased and then increased reversely. The local airflow

movement played a dominant role in the strain after the difference between internal and external pressure decreased. In the fifth stage, with the decrease of relative vacuum degree, the tensile strain increased. The pressure difference changed slowly in the initial stage of natural venting, so the effect of the local airflow was still dominant. In the sixth stage, with the decrease of relative vacuum degree, the tensile strain decreased. The difference between internal and external pressure approached to zero, as well as the strain returned to zero.

As can be seen from the above, both local airflow movement and pressure difference had an impact on the surface strain of the segment concrete, and dominated by turns in different stages of vacuum discharge.

*4.2. Displacement Monitoring.* The curve of the joint distance along with time is shown in Figure 17. The Displacement meter DZZ is installed at the longitudinal joint of the adjacent segments, while the displacement meter DZH is installed at the ring joint of the adjacent segments.

It can be seen from Figure 17 that the joint spacing between adjacent segments decreased with the increasing vacuum and increased with the vacuum pressure relief. In this process, the increase of the segment ring shrinkage was induced by an increase of pressure difference. The maximum variation of the joint spacing was 0.205 mm~0.555 mm.

*4.3. Steel Gauge Monitoring.* It was found from the monitoring data that the peak frequency of the steel bar meter at each measuring point was observed at the beginning, then it decreased with the increase of the vacuum pressure, implying that the steel bar was always compressed. Several typical monitoring point data are shown in Table 1.

It can be seen from Table 1 that the stress of the inner circumferential steel bar (K2, 1A2, 1A9, 2A2, 3A2) was significantly greater than that of the outer steel bar, and the stress of the steel bar (3A2, 1A2) near the joint of the segment was significantly smaller than that at other locations due to the cushioning effect of the elastic gaskets between the adjacent segments. Compared with the design compressive strength of 360 $N/mm^2$ of HRB400 steel bar, the maximum stress of the steel bar caused by vacuum was very small, about 0.1‰, which may be ignored.

*4.4. Concrete Strain Gauge Monitoring.* Noting that the peak frequency of the concrete strain gauge at each measuring point was observed at the beginning, and then the frequency decreased with the increase of the vacuum pressure. The concrete was always compressed similarly. Several typical monitoring point data are shown in Table 2.

It can be seen from Table 2 that the strain value of concrete was small. Compared with the ultimate compressive strain (0.0033) of concrete, the maximum strain caused by vacuum only accounted for about 6‰.

## 5. Conclusions and Recommendations

Focusing on the sealing reliability and mechanical behavior of assembled tunnel prototype segments under low vacuum conditions, a prototype segment low vacuum test system has been designed and built in this paper, which can simulate internal vacuum and external environmental pressure. Based on the test platform, the sealing capacity and mechanical properties of the segment under low-vacuum complex environment are studied in this paper, and the following conclusions are obtained:

(1) The longitudinal assembly force is more conducive to improving the air tightness of the structure than the transverse one. When the compression force of the sealing gasket is 80 kN/m, the relative vacuum maximum of the two ring segments is 43 kPa with a pumping rate of 200 $m^3$/h. Therefore, the sealing of the current concrete segment structure needs to be further strengthened

(2) The longitudinal and circumferential strain of the concrete segment are consistent. The maximum tensile strain on the concrete surface caused by the local airflow movement of vacuum pumping is about 55% of the ultimate tensile strain of the concrete, which needs to be paid attention to. The reinforcement by spraying concrete surface is recommended

(3) The surface strain of concrete is affected by both local airflow movement and pressure difference between internal and external, which take turns in dominance in different stages of vacuum discharge

(4) The relative pressure caused by vacuum has little effect on the stress and deformation of the structure. The strain caused by vacuum only accounts for 6‰ of the ultimate compressive strain of concrete, while the stress of the steel accounts for 0.1‰ of the steel design compressive strength, which can be ignored. When vacuumizing, the relative pressure between the inside and outside structure causes the joint space to decrease slightly by 0.555 mm

In this paper, the sealing performance and mechanical behavior of the existing tunnel assembly segment in a low vacuum environment have been obtained in the prototype test, which provides the experimental basis for the pipeline design of the low vacuum pipeline transportation system. In the later stage, the sealing performance of the existing assembly segment structure will be improved, the ultimate vacuum degree inside the structure will be further improved, and related structural performance research will be carried out.

## Data Availability

The data that support the findings of this study are available from the corresponding author upon reasonable request.

## Conflicts of Interest

The authors declare that they have no conflicts of interest.

## Authors' Contributions

Conceptualization was done by Qianqian Lv and Chuigang Zeng. The methodology was performed by Qianqian Lv, Fengyuan Li, and Kui Chen. Formal analysis and investigation were executed by Qianqian Lv, Long Shi, and Ruixiang Chen. Writing the original draft preparation was done by Qianqian Lv. Writing—review and editing were performed by Qianqian Lv, Kui Chen, and Long Shi. The funding acquisition was done by Chuigang Zeng and Fengyuan Li.

## Acknowledgments

This work was supported by the Science and Technology Research and Development Program of China Railway Corporation Limited (No. 2020-Zhongdian-27) and Science and Technology Innovation Plan of China Railway Tunnel Bureau Group (Suiyanhe 2019-08).

## References

[1] Z. Y. Shen, "On developing high-speed evacuated tubetransportation in China," *Journal of Southwest Jiaotong University*, vol. 40, no. 2, p. 133, 2005.

[2] J. Sun, Z. Z. Liu, and J. P. Liu, "Great revolution in maritime transportation: discussion on preliminary work and operation plan of bridge/tunnel projects for vacuum HTS maglev train at high speed," *Tunnel Construction*, vol. 38, no. 9, p. 1405, 2018.

[3] Z. G. Deng, Y. Zhang, and B. Wang, "Present situation and prospect of evacuate tube transportation system," *Journal of Southwest Jiaotong University*, vol. 54, no. 5, p. 1063, 2019.

[4] Z. W. Feng, X. Fang, and H. M. Li, "Technological development of high speed maglev system based on low vacuum pipeline," *Engineering Sciences*, vol. 20, no. 6, p. 105, 2018.

[5] Y. P. Zhang, "High-speed railway route scheme of submarine vacuum tube from Yantai to Dalian," *Tunnel Construction*, vol. 40, no. 3, p. 299, 2020.

[6] N. A. Alexander and M. M. Kashani, "Exploring bridge dynamics for ultra-high-speed, hyperloop, trains," *Structure*, vol. 14, pp. 69–74, 2018.

[7] D. Oster, M. Kumada, and Y. Zhang, "Evacuated tube transport technologies (ET3) tm; a maximum value global transportation network for passengers and cargo," *Journal of Modern Transportation*, vol. 19, no. 1, pp. 42–50, 2011.

[8] A. S. Abdelrahman, J. Sayeed, and M. Z. Youssef, "Hyperloop transportation system: analysis, design, control, and implementation," *Transactions on Industrial Electronics*, vol. 65, no. 9, pp. 7427–7436, 2018.

[9] T. H. Heaton, "Inertial forces from earthquakes on a Hyperloop pod," *Bulletin of the Seismological Society of America*, vol. 107, no. 5, pp. 2521–2524, 2017.

[10] J. Braun, J. Sousa, and C. Pekardan, "Aerodynamic design and analysis of the hyperloop," *AIAA Journal*, vol. 55, no. 12, pp. 4053–4060, 2017.

[11] A. Santangelo, "Hyperloop as an evolution of maglev," *Transport System Technology*, vol. 4, no. 4, pp. 44–63, 2018.

[12] S. P. Kaushal, "Hyperloop: fifth mode of transportation," *International Journal of Engineering Science*, vol. 4, pp. 274–278, 2020.

[13] M. Rosenmayr, A. Cassat, and H. Stemmler, "SWISSMETRO Ector control for a homopolar synchronous linear motor. International conference on MAGLEV 2000, Rio de Janeiro (6)7," in *Proceedings of the International conference on MAGLEV*, 2000.

[14] A. Cassat, V. Bourquin, and M. Mossi, "SWISSMETRO project development status," in *Proceedings of the International Symposium on Speed-up and Service Technology for Railway and Maglev Systems 2003*, pp. 410–453, Tokyo, Japan, 2003.

[15] "Transpod. Test Half-Scale Test Track in Droux. Transpod 2021," April 2021, http://www.transpod.com/test-facility//.

[16] Z. G. Deng, W. H. Zhang, J. Zheng et al., "Ahigh temperature super conducting maglev ring test line developed in Chengdu, China," *IEEE Transactions on Applied Superconductivity*, vol. 26, no. 6, p. 3602408, 2016.

[17] Z. Deng, W. Zhang, J. Zheng et al., "A high-temperature superconducting maglev-evacuated tube transport (HTS maglev-ETT) test system," *IEEE Transactions on Applied Superconductivity*, vol. 27, no. 6, article 3602008, 2017.

[18] B. Wang, *Study on Aerodynamic Characteristics of Evacuated Tube Transport-High Temperature Superconducting Maglev*, Southwest Jiaotong University, Chengdu, 2017.

[19] Q. Lv, Z. Sun, and J. Zhou, "Experimental study on mechanical behavior and sealing performance of low vacuum tunnel structure," *Tunnel Construction*, vol. 40, no. 4, p. 496, 2020.

[20] C. J. Gong, Y. Y. Wang, Y. C. Peng et al., "Three-dimensional coupled hydromechanical analysis of localized joint leakage in segmental tunnel linings," *Tunnelling and Underground Space Technology*, vol. 130, article 104726, 2022.

[21] M. F. Lei, B. B. Zhu, C. J. Gong, W. Ding, and L. Liu, "Sealing performance of a precast tunnel gasketed joint under high hydrostatic pressures: site investigation and detailed numerical modeling," *Tunnelling and Underground Space Technology*, vol. 115, article 104082, 2021.

[22] P. Devkota and J. Park, "Analytical model for air flow into cracked concrete structures for super-speed tube transport systems," *Infrastructures*, vol. 4, no. 4, p. 76, 2019.

[23] C. H. Park, J. H. Synn, and J. Park, "Probabilistic performance assessment of airtightness in concrete tube structures," *KSCE Journal of Civil Engineering*, vol. 20, no. 4, pp. 1443–1451, 2016.

[24] Q. Q. Lv, "Model experimental research on the temperature stress of low vacuum pipeline structure," *Journal Of Railway Engineering Society*, vol. 39, no. 1, p. 18, 2022.

[25] Q. Lv, Z. Sun, and J. Zhou, "Laboratory experiment on the system performance of low vacuum piping," *Vacuum*, vol. 58, no. 3, p. 7, 2021.

[26] C. J. Gong, L. Kang, L. H. Liu, M. Lei, W. Ding, and Z. Yang, "A novel prediction model of packing density for single and hybrid steel fiber-aggregate mixtures," *Powder Technology*, vol. 418, article 118295, 2023.

[27] Y. Zhang, *Study on Aerodynamic Characteristics of Maglev Transport System with a Low-Pressure Tube*, Southwest Jiaotong University, Chengdu, 2019.